

High Performance All-2D Layered Tin Disulfide:Graphene Photodetecting Transistors with Thickness Controlled Interface Dynamics

Ren-Jie Chang,¹ Haijie Tan,¹ Xiaochen Wang,¹ Benjamin Porter,¹ Tongxin Chen,¹ Yuewen Sheng,¹ Yingqiu Zhou,¹ Hefu Huang,¹ Harish Bhaskaran,¹ Jamie H. Warner^{1}*

¹Department of Materials, University of Oxford, Parks Road, Oxford, OX1 3PH, United Kingdom

Email: Jamie.warner@materials.ox.ac.uk

Abstract

Tin disulfide crystals with layered 2D sheets are grown by chemical vapor deposition (CVD) using a novel precursor approach and integrated into all 2D transistors with graphene (Gr) electrodes. The Gr:SnS₂:Gr transistors exhibit excellent photodetector response with high detectivity and photoresponsivity. We show that the response of the all 2D photodetectors depends upon the charge trapping at the interface and the Schottky barrier modulation. Thickness dependent SnS₂ measurements in devices reveal a transition from interface dominated response for thin crystals to bulk like response for the thicker SnS₂ crystals, showing the sensitivity of devices fabricated using layered materials on the number of layers. These results show that SnS₂ has photosensing performance when combined with graphene electrodes that is comparable to other 2D transition metal dichalcogenides of MoS₂ and WS₂.

KEYWORDS: SnS₂, Graphene, Photodetectors, transistors, vertical layered heterostructures, 2D, TMDs, Schottky barrier height.

Introduction

The thriving graphene research over the past decade has expanded into the development of other two-dimensional (2D) materials with complementary electronic properties.¹⁻² Monolayer molybdenum disulfide (MoS_2) and tungsten disulfide (WS_2) are examples of semiconducting transition metal dichalcogenides (TMDs),³ which have a bandgap in the red spectral region (1.8~2.0 eV) and several fascinating physical properties including piezoelectricity,⁴ spin-orbit interaction and valley hall effect.⁵⁻⁶ Additionally, the direct bandgap,⁷ high absorption coefficient and 2D structural form makes them promising candidates for flexible optoelectronic application such as phototransistors,⁸ light emitting diodes (LED),⁹ memory devices and logic circuits.¹⁰⁻¹¹ For the purpose of optoelectronic devices with greater selectivity in wavelength, it is essential to develop other 2D layered semiconductors with bandgaps that could cover the entire visible spectrum. 2D semiconducting materials with blue and green light absorption have therefore been exploited in the past few years. For example, metal monochalcogenide gallium sulfide (GaS) has reported to exhibit a bandgap of 2.5 eV when reducing to monolayer,¹² which is appropriate for blue light channel. In comparison, 2D indium selenide (InSe), gallium selenide (GaSe) and tin disulfide (SnS_2) are ideal candidates for green light channel, with the bandgap of 2.4 eV,¹³ 2.1 eV and 2.2 eV,¹⁴⁻¹⁵ respectively.

SnS_2 is particularly of great interest among the layered materials due to its earth-abundant and environmentally-friendly constituents with prominent chemical stability. Similar to MoS_2 , SnS_2 exhibits n-type characteristics and possesses a layered structure, but with tetragonal (T) phase as the most stable crystal structure phase in comparison with the hexagonal (H) phase in MoS_2 . It crystallizes in a CdI_2 -type lattice structure, in which S-Sn-S trilayers with internal covalent bondings are held together by van der Waals forces. The S-Sn-S trilayers are stacked with a periodicity of one layer and a global D_{3d} space group symmetry. Recent studies have also demonstrated the great potential of SnS_2 in various application including field effect

transistors with high carrier mobility and on-off ratio,¹⁶ gas sensors with high sensitivity and selectivity,¹⁷ thermoelectric devices with high conversion efficiency,¹⁸ and anodes with high charge storage capacity for Na/Li ion batteries.¹⁹ It is also predicted that SnS₂ could be a potential stabilizer for the metallic phase in monolayer MoS₂ and WS₂ through alloying,²⁰ which is beneficial for better catalytic activity in electrochemistry and energy storage. In addition, it is observed that the removal of sulfur atoms under the electron irradiation of SnS₂ results in phase transformation into p-type SnS semiconductor,²¹ which could enable the direct synthesis of lateral p-n junction with sharp interface simply by using tin chalcogenides component.²²

Photodetector is one of the application of SnS₂ that shows promising potential. Huang et al. firstly used the mechanical exfoliated few-layer SnS₂ to fabricate photodetecting transistor and demonstrated a photoresponsivity of ~100 A/W.²³ Similarly, Tao et al. later developed a chemical hot bath method for the synthesis of SnS₂, and the resulted photodetector showed a high spectral selectivity. However, the lack of scalability hinders these top-down approaches from industrial mass production.²⁴ In comparison, chemical vapor deposition (CVD) is the effective way to achieve large area growth of atomically thin 2D materials for the successful device application. The CVD growth of MoS₂ and WS₂ has been well-investigated, the domain size could be at the scale of 100 μ m and the growth of continuous films with high uniformity could also be achieved.²⁵⁻²⁷ In light of this, Su et al. reported a controlled CVD growth of SnS₂ on SiO₂ with patterned seed array. The as-fabricated photodetectors exhibit a short respond time ~5 μ s, which is much faster than other layered 2D semiconductors. The CVD-grown SnS₂ with different morphology has been subsequently demonstrated on other growth substrate and integrated on polymer film for flexible photodetectors.²⁸⁻²⁹ Photodetecting devices incorporating van der Waals (vdW) crystals with SnS₂ layers and other 2D materials, however, has not been reported yet. This may be ascribed to the complex

fabrication process including multiple lift-off and etching procedures to pattern 2D materials without damaging their adjacent layers.

In this study, we for the first time demonstrate the use of combination of SnS₂ with graphene (Gr) to fabricate Gr:SnS₂:Gr lateral heterostructures and investigate their photodetecting performance. All the 2D materials are obtained from CVD growth, which has the advantages for scalable production in the future compared to previous report using mechanical exfoliation.³⁰ The adjustable Fermi level of graphene could modulate the Schottky barrier height and lower the contact resistance at Gr-SnS₂ interface, giving rise to high photoresponsivity (~ 20 A/W) and detectivity (4×10^{14} Jones). The thickness of SnS₂ channel is also found to be influential on detecting behavior- turning from interface dominant to bulk dominant as the thickness of SnS₂ increases. These appealing features provide SnS₂-based photodetectors a bright future for the applications of flexible optoelectronics.

Results and discussion

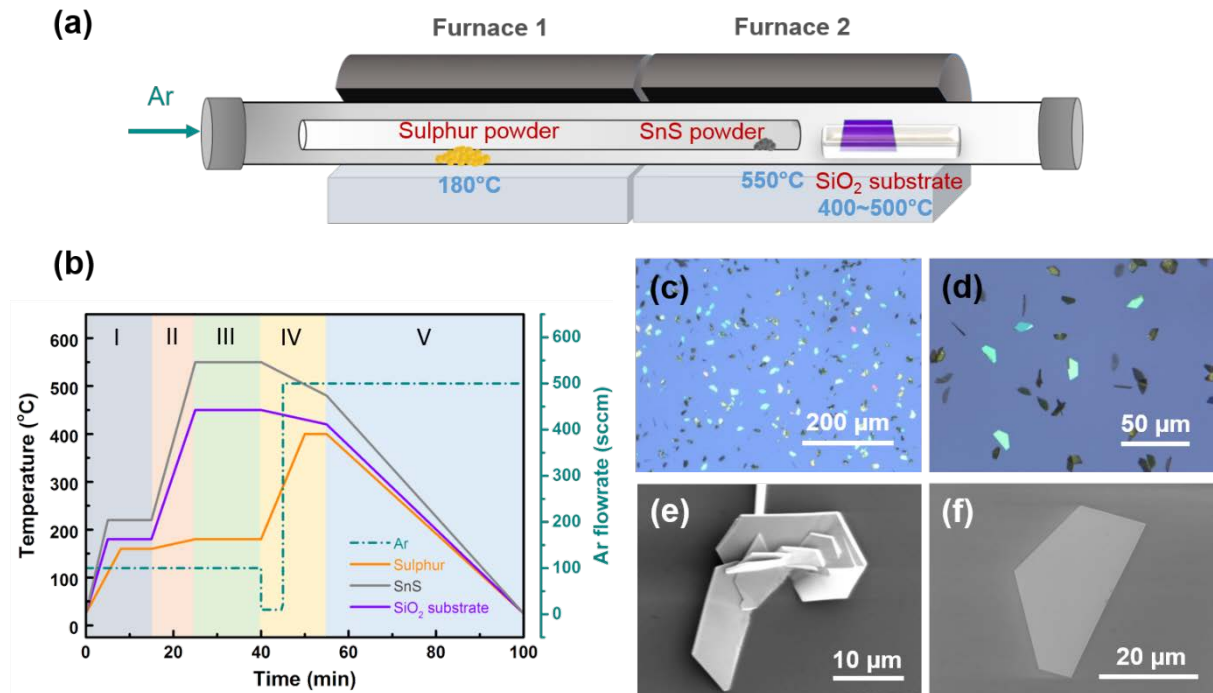


Figure 1. Atmospheric pressure CVD synthesis of SnS₂ crystals on SiO₂ substrate. (a) Schematic illustration of the CVD experimental set-up for synthesizing SnS₂ crystals. (b) Temperature and carrier gas profile for the CVD growth. There are five stages included in the whole process: (I) Sulphur pre-introduction, (II) heating, (III) growth, (IV) slow cooling and (V) fast cooling. (c) A low-magnification optical image to show the large-scale production of as-grown SnS₂ crystals. (d) The enlarged view of optical image showing the details of thin and thick SnS₂ crystals. (e-f) SEM images of SnS₂ crystals grow in the (e) perpendicular and (f) horizontal directions to the SiO₂ substrates, respectively.

Figure 1(a) schematically illustrates the CVD setup for the CVD growth of SnS₂ with SiO₂ substrate placing on the ceramic crucible. SnS₂ was grown by using tin sulfide (SnS) and sulfur precursors. Sulfur and SnS precursors are placed in the center of furnace 1 and 2, respectively, while the SiO₂ substrate are put at the downstream of furnace 2, around 6 cm away from the SnS powders. Compared to conventional tin precursor using tin dioxide (SnO₂) for the synthesis of SnS₂, SnS precursor could reduce the thermal budget of CVD growth as the bonding energy of Sn-S is lower than that of Sn-O bonding.³¹ Besides, the absence of oxygen in the precursor is also beneficial for the growth of high crystallinity without oxygen defects. The SnS₂ growth was carried out using a custom designed 1-inch CVD system with quartz tube and gas flow rates controlled by digital mass flow controllers. The two separate furnaces provide better control of both precursors and substrate. With a view to avoiding unnecessary reactions between two different precursors during vaporized atoms transport to the substrate, two concentric quartz tubes were used to separate the gaseous precursors before they reached to substrate surface. The detailed of growth parameter setting is displayed in Figure 1(b). At the beginning of the growth, both the furnace temperatures was raised over 180°C for 15 min with 100 sccm Ar carrier gas to provide sulphur-rich environment for the whole CVD reactor. The furnace 2 was then heated up to 550°C, followed by a 15 min SnS₂ growth. After the growth, the flow rate of Ar was set down to 10 sccm and the furnace 1 was raised to 400°C to evaporate the residual Sulphur powders. Those excess Sulphur vapor was

purged away by turning back the flow rate of Ar to 500 sccm when the temperature of furnace 2 was lower than 500°C. The fast cooling was carried out after the purging of Sulphur vapor to stop the CVD growth process. By optimizing the growth parameters, which will be discussed later, the high-quality of layered SnS_2 crystals with different thickness could be obtained. Figure 1(c) and (d) are the low-magnification and high-magnification optical images of the as-grown SnS_2 crystals, respectively. It is noted that except growing along the planar directions (Figure 1(e)), part of the SnS_2 crystals are grown in out-of-plane directions and stand semi-vertically (Figure 1(f)). This may be attributed to the large amount of dangling bonds on the SiO_2 surface, resulting in larger energy barrier for surface diffusion and shorter diffuse length of the Sn-S active species.

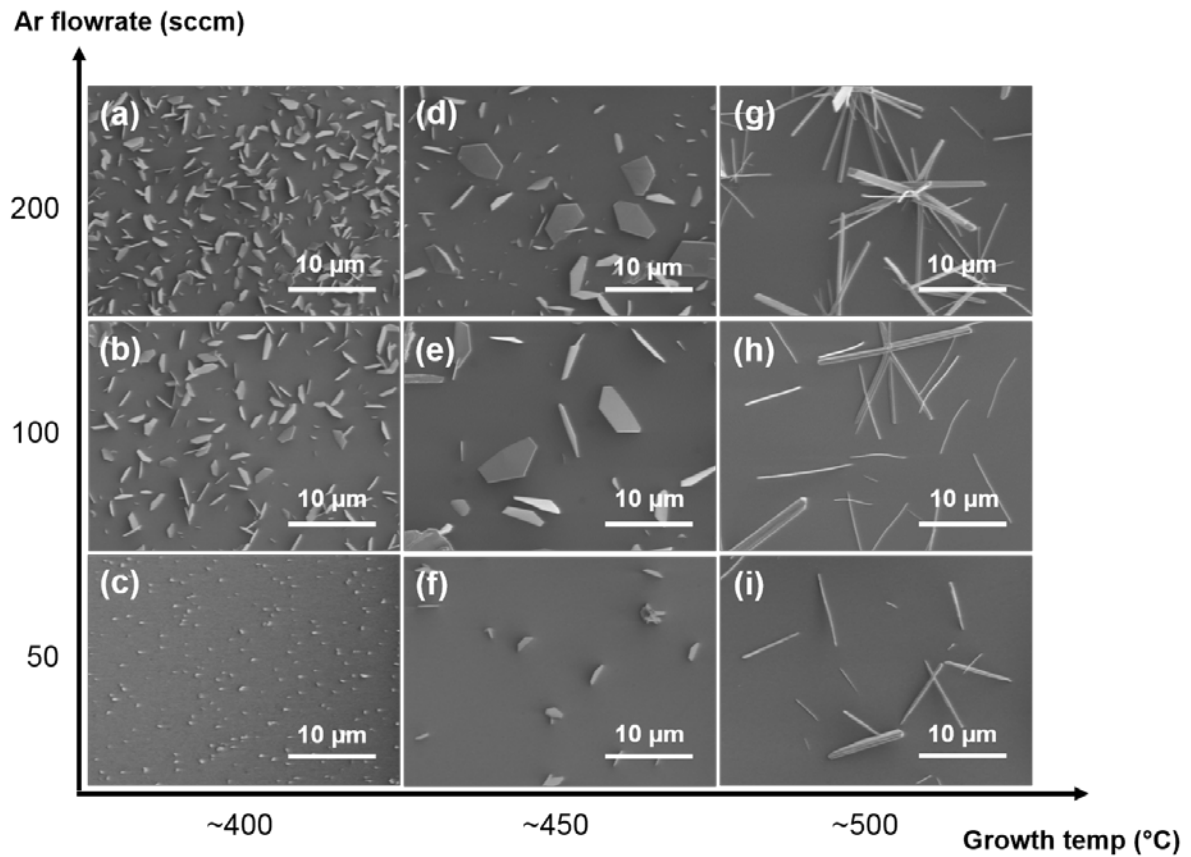


Figure 2 SEM images demonstrating the morphology control of SnS₂ growth under different growth conditions in terms of T(°C)/J_{Ar}(sccm): (a) 400/200, (b) 400/100, (c) 400/50, (d) 450/200, (e) 450/100, (f) 450/50, (g) 500/200, (h) 500/100 and (i) 500/50.

In the typical CVD growth, there are five elementary steps including: (1) the sublimation of precursors and the transport of gas molecules to the substrate, (2) diffusion of the molecules through the boundary layer and adsorption of molecules onto the substrate surface, (3) surface diffusion of the active species, (4) attachment to the growth sites that are thermally stable, (5) desorption of the excess active species. Generally, the rate limiting step in the whole growth process could be either diffusion (step (2)) or reaction on substrate surface (step (3) and (4)), which is strongly affected by flow rate of carrier gas and reaction temperature, respectively. To obtain SnS₂ crystals with high quality, we systematically optimize the growth of SnS₂ through tuning these crucial parameters as reported in Figure 2. As shown in Figure 2(g), (h) and (i), the growth begins to transfer from nanoplatelets to nanowires when the growth temperature is above 500°C. The Raman spectrum for these nanowires shown in Figure S1 exhibits the characteristic peaks located at 153.5 cm⁻¹, 235.2 cm⁻¹ and 309.1 cm⁻¹. This is corresponding to other report in Sn₂S₃ growth, indicating the existence of Sn₂S₃ under higher growth temperature.³² The growth of SnS₂ is preferential under the growth temperature below 500°C, leading to the growth in planar direction the crystal morphology become trapezoid, which is similar to previous report. The low rate of Ar carrier gas is found to be influential to the growth direction. As shown in Figure 2(d-f), high Ar flow rate will produce larger percentage of the SnS₂ crystals growing along out-of-plane directions, while low Ar flow rate could lower the reaction rate of the tin and sulfur precursors. This phenomenon could be ascribed to the different mass transfer rate in the CVD growth. Under the high Ar flow rate the adsorbed species on SiO₂ substrate may not have enough time to incorporate into the lattice site that is most thermodynamically stable. The SnS₂ crystals

therefore have higher tendencies to grow with out-of-plane directions. The low Ar flow rate, in comparison, results in larger boundary layer thickness for mass transport and restricts the precursor supplies. Through the growth parameters optimization, the moderate growth temperature and the Ar carrier flow rate could lead to a better growth of SnS₂ crystals. The SnS₂ crystals with domain size around 20 μm and thickness of 10-30 nm could be obtained under the 450°C and Ar flow rate of 100 sccm.

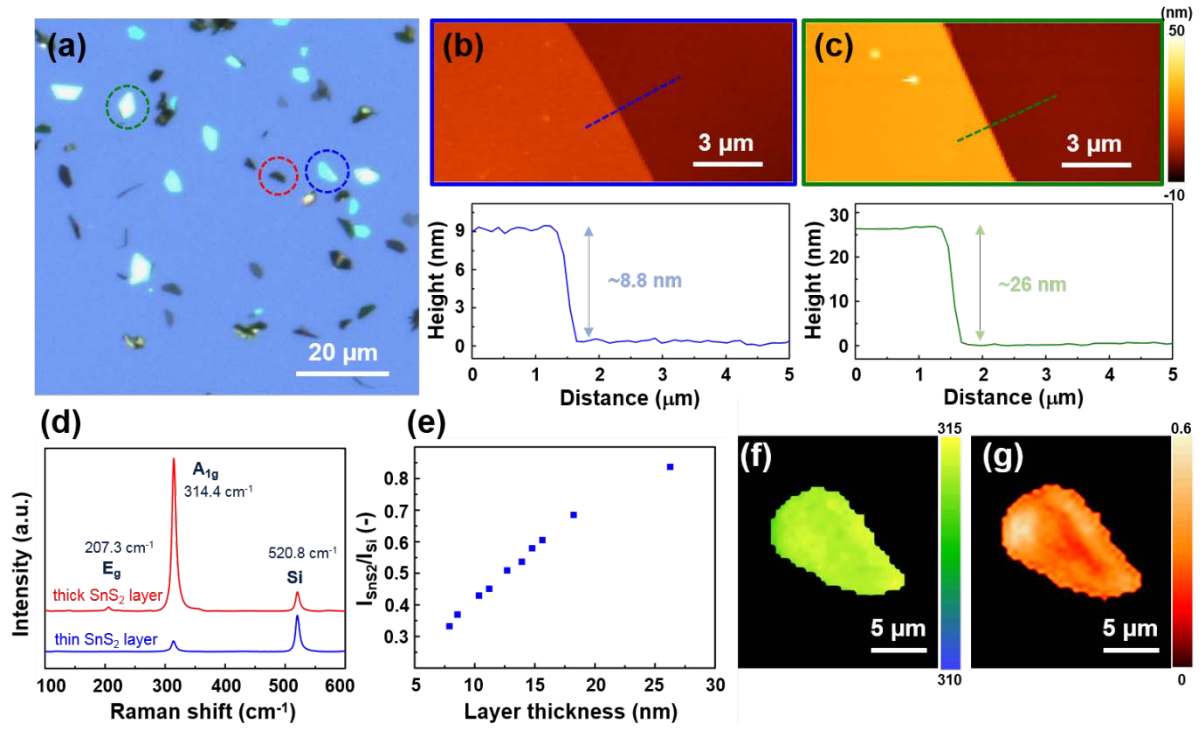


Figure 3. Raman analysis and atomic force microscopy (AFM) of SnS₂ crystals. (a) Optical image displaying the distribution of SnS₂ crystals with different thickness. (b-c) AFM images and height profiles of SnS₂ crystals with different thickness indicated by blue and green dashed circle, respectively, in (a). (d) Raman spectrum of SnS₂ crystals with different thickness indicated by blue and red dashed circle, respectively, in (a). (e) The relationship between the intensity ratio of SnS₂ A_{1g} peak and Si characteristic peak from Raman spectrum and the layer thickness measured by AFM. (f) Raman mapping for the peak position of A_{1g} mode from SnS₂ crystal indicated in the blue dashed circle in (a). (g) Raman mapping for the peak intensity ratio between A_{1g} mode from the same SnS₂ crystal and Si substrate.

To determine the thickness of individual SnS₂ crystals, we perform the atomic force microscopy (AFM) study. Figure 3(a) shows the as-grown SnS₂ crystals with a variety of thickness. The measured AFM thickness of the crystals in blue and green dashed circle are listed in Figure 3(b) and (c). Raman spectrum was further adopted to characterize the SnS₂ crystals with different thickness. As shown in Figure 3(d), there are two Raman characteristic peak of SnS₂, A_{1g} at 314 cm⁻¹ and E_g at 207 cm⁻¹, corresponding to the out-of-plane vibrational

phonon mode and the intra-layer vibrational phonon mode.³³ The E_g peak disappears as decreasing the layer number due to the reduction in the number of scattering center for the in-plane scattering. In addition, the absence of A_g and B_{3g} peaks confirms that the SnS precursor was fully converted into SnS₂ on the SiO₂ substrates.³⁴ To quantify thickness dependence, we combine the AFM measurement with Raman analysis, as shown in Figure S2, each SnS₂ characteristic peak from spectrum was normalized by the intensity of Si peak. It can be seen from Figure 3(e) that the intensity ratio of A_{1g} peak and Si peak increases approximately linearly with thickness, which is consistent with the previous simulation report using first-principles calculation method.³⁵ This enables Raman analysis to serve as a simple approach for measuring the layer number. To elucidate the uniformity of individual SnS₂ domain, the SnS₂ crystal marked by blue dashed circle in Figure 3(d) was further analyzed by Raman mapping. The A_{1g} peak position mapping from Figure 3(f) shows that the all the SnS₂ crystal positions exhibit a characteristic peak centered around 313.5 cm⁻¹ to 314.5 cm⁻¹, indicating the composition uniformity. From Figure 3(g) demonstrating the mapping for intensity ratio of A_{1g} peak to Si characteristic peak, it can be seen that the area near the crystal edge has slightly larger value. This could be resulted from the defects near the SnS₂ crystal edges that accelerate the adlayer growth.

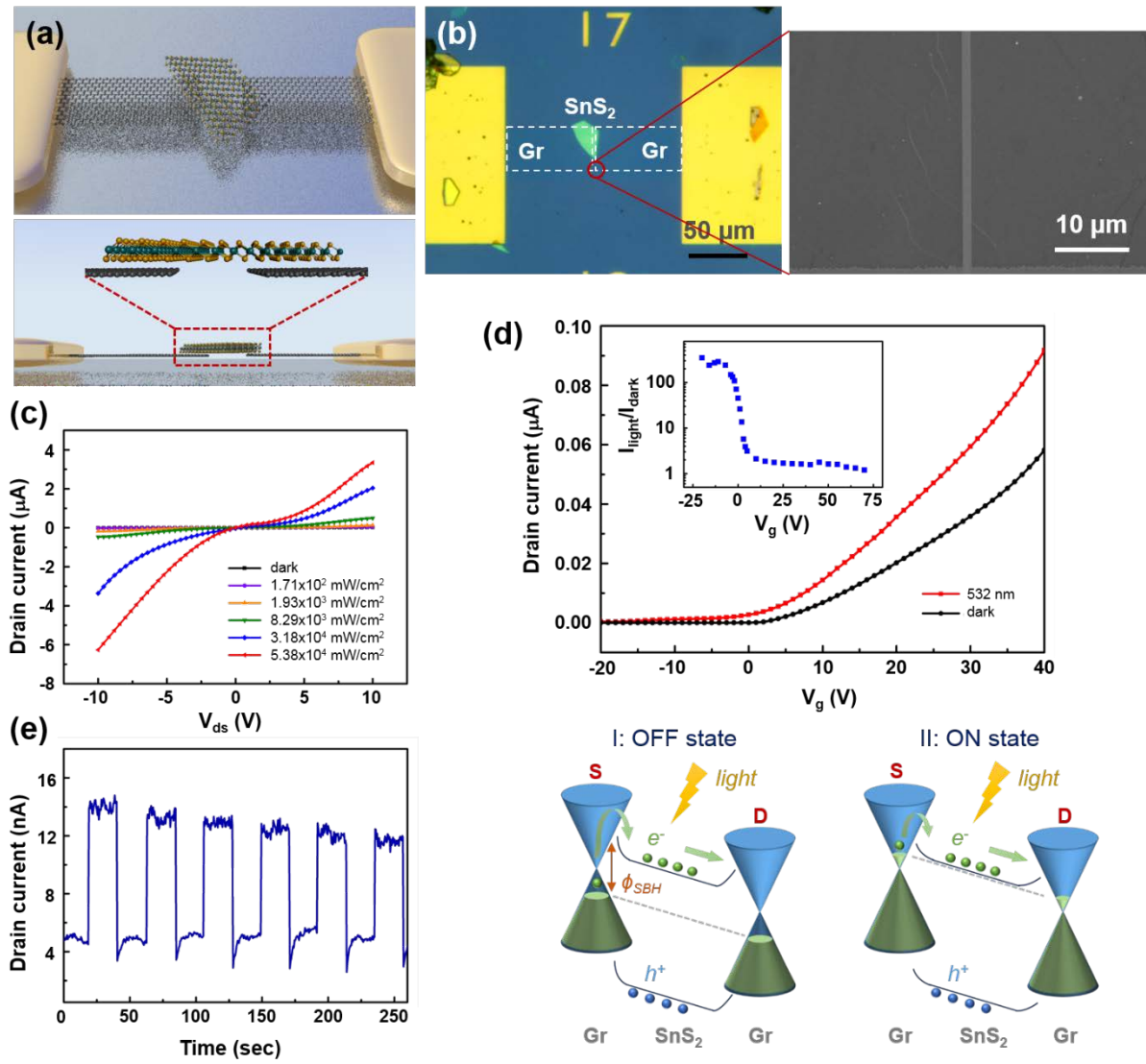


Figure 4. Characteristics of SnS₂-based photodetectors. (a) Schematic illustrations of fabricated photodetector with SnS₂ crystals on patterned graphene ribbons. (b) Optical image of a fabricated single Gr-SnS₂-Gr photodetector. The magnified SEM image shows the gap between graphene electrodes is 1 μm . (c) I-V curve of the Gr-SnS₂-Gr device in the dark and in the presence of laser illumination with different intensities. (d) Comparison of the transfer curves for Gr-SnS₂-Gr photodetector measured in the dark and under the illumination at 171 mW/cm^2 and under 5 V biased voltage. The inset shows the photoresponse ratio of the illumination current and dark current as a function of gate bias. The bottom illustration displays the band diagram of the SnS₂ photodetector at the graphene electrode contacts when tuning the gate

voltage at ON and OFF state. (e) Photoswitching behavior of the device resulted from the incident pulsed laser light with intensity $2.55 \times 10^4 \text{ mW/cm}^2$ under bias of 2 V.

To further evaluate the quality of as-grown SnS₂ crystals, we fabricated SnS₂ photodetector through using PMMA supporting layer to transfer the as-grown SnS₂ onto the graphene ribbon, the detail is described in the Experimental Section. Figure 4(a) schematically shows the top view and the side view of the SnS₂ photodetector with the graphene electrodes connected to the Cr/Au bond pads. Figure 4(b) shows the optical image of such a device that includes the SnS₂ crystals bridging between the graphene electrodes. The gap between the graphene electrodes is measured to be 1 μm . The quality of graphene electrodes is identified by Raman spectrum shown in Figure S3(a), the intensity of 2D peak twice larger than G peak and the absence of D peak indicates the monolayer graphene with high quality. Figure 4(c) displays the output characteristic of the device, the IV measurement both under the dark state (Figure S3(b)) and laser illumination is notably nonlinear and asymmetric with respect to the bias polarity, indicating the Schottky contact between the graphene electrode and the SnS₂ channel. The dependence of current profile on the back-gate voltage is also investigated. As shown in Figure S3(c), the transfer characteristics of the device demonstrate the n-type behavior with higher conductance at higher gate voltage. The device remains its n-type characteristics under the laser illumination, and the drain current is larger than that in the dark for all applied gate voltage and increases significantly when sweeping the gate voltage to the on state, shown in Figure 4(d). This indicates the photocurrent dominates over thermionic and tunneling current in the whole operation of the device. The influence of gate voltage on photoresponse ratio, demonstrated in the inset of Figure 4(d), is further investigated. As switching the gate voltage to the OFF state, the ratio is much higher than that in the ON state, indicating that more tunneling and thermionic current participate in the SnS₂ channel with the increase of gate voltage. Therefore, the photocurrent predominates the channel current when

the device is in the OFF state. The principle was also explained by the energy band diagram of the SnS₂ photodetector, shown in the bottom of Figure 4(d). The work function of graphene is estimated around 4.6 eV and the electron affinity of SnS₂ is about 4.1 eV,³⁶⁻³⁷ resulting the formation of Schottky barrier at the interface between graphene and SnS₂. When the device is in the depletion region, the down-shifted Fermi level of SnS₂ results in a large energy barrier between the conduction band of SnS₂ and the Fermi level of graphene. As a consequence, upon illumination, the photocurrent in the SnS₂ channel outnumbered the tunneling and thermionic current. By contrast, when the device is operated in the accumulation region, the tunneling and thermionic current can easily overcome the barrier because the Fermi level approached its conduction band.³⁸ The reduction of the energy barrier also allows a more efficient generation of photocurrent and stronger photoresponse. In addition, the photoswitching characteristics demonstrated in Figure 4(e) shows the SnS₂ photodetector exhibit a stable and reproducible photoresponse in a series of periodical light stimulation. It is noted that the high off current and low on-off current ratio could stem from the lower contact resistance between graphene and SnS₂ layers, further improvement via revising device configuration may be adopted in the future.

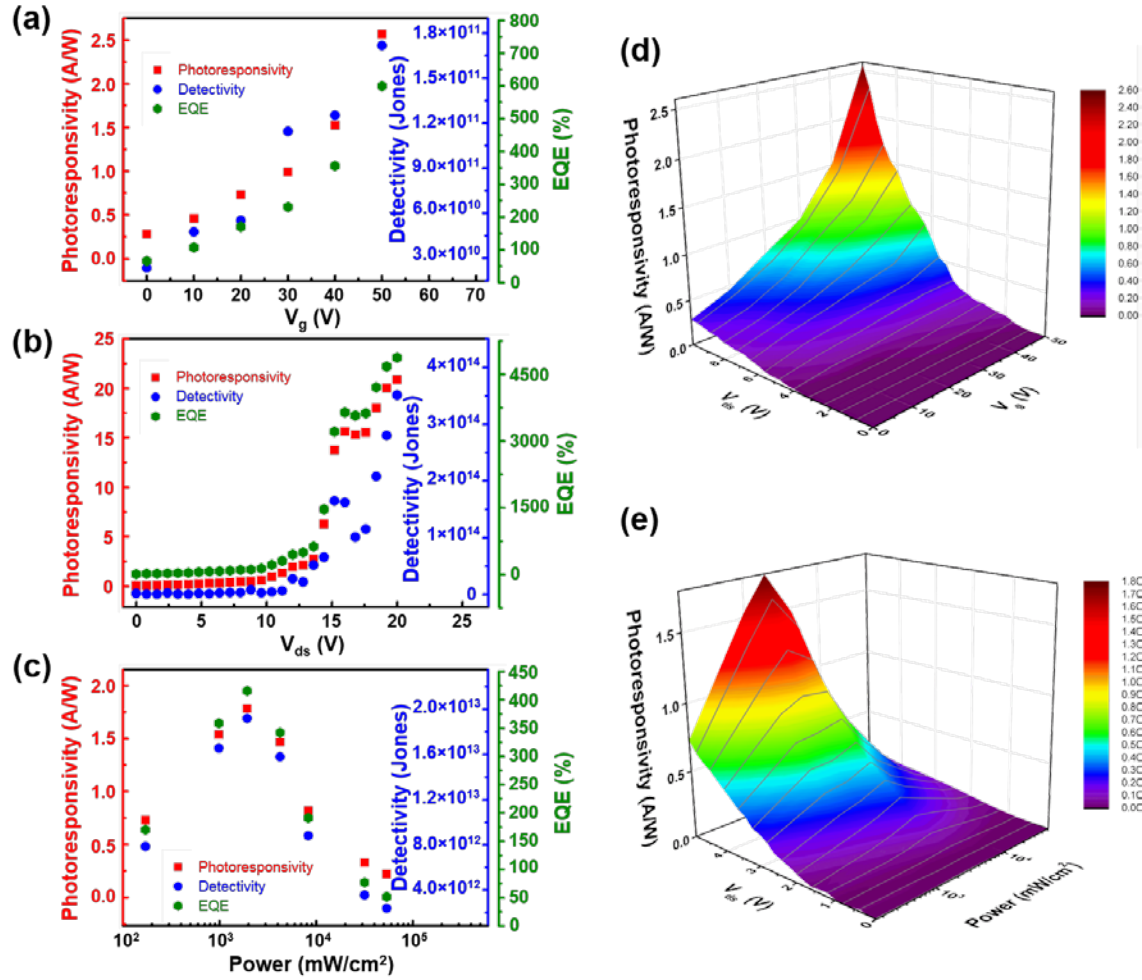


Figure 5. Photodetection performance of Gr-SnS₂-Gr under the influence of gate, illumination power and source-drain bias. (a) Influence of gate bias on photoresponsivity, detectivity and external quantum efficiency (EQE) for the SnS₂ device. (b) Influence of source-drain bias on photoresponsivity, detectivity and EQE for the SnS₂ device. (c) Influence of illumination power on photoresponsivity, detectivity and EQE for the SnS₂ device. (d) The 3D view of photoresponsivity mapping for the Gr-SnS₂-Gr photodetector under different source-drain bias and gate bias. (e) The 3D view of photoresponsivity mapping for the Gr-SnS₂-Gr photodetector under different source-drain bias and laser illumination.

To further characterize the performance of the device, we continue to discuss other three main figures of merit that are used to evaluate the behavior of photodetection. Photoresponsivity (R), defined as the ratio of output photocurrent to the input optical power,

represents the device electrical response to the incident light at a certain wavelength. In Figure 5(a), photoresponsivity rises with the gate voltage sweeping to the positive side. The calculated photoresponsivity at $V_G = 50$ V is about 10 times greater than that at $V_G = 0$ V. External quantum efficiency (EQE) is the ratio between the number of photogenerated carriers and the number of incident photons, it can be expressed by using following formula:

$$EQE = hcR/e\lambda \quad (1)$$

where h is Plank's constant, c is the light velocity, R is the photoresponsivity, e is the elementary charge and λ is the wavelength of incident light. In addition, taking the bandwidth, geometry and noise of the device into consideration, specific detectivity (D^*) reflects the sensitivity of the device. It is defined by $D^* = R \times (Af)^{1/2} / i_N$, where A is the effective area of the detector, f is the bandwidth, and i_N is the noise current of the device. By considering the shot noise as the main noise source with $i_N = (2eI_{dark})^{1/2}$, D^* can be consequently expressed as

$$D^* = RA^{1/2} / (2eI_{dark})^{1/2} \quad (2)$$

where I_{dark} is the measured dark current. It is worthwhile noting that the device based on 2D materials contains a $1/f$ noise component resulted from the non-Ohmic contacts and defects that are non-negligible.³⁹⁻⁴⁰ Similar to photoresponsivity, both EQE and detectivity increase when sweeping the gate voltage toward the ON state due to the enhanced carrier mobility. As shown in Figure 5(b), all the photoresponsivity, EQE and detectivity increase with the enhancement of source-drain bias, this is because of the higher carrier concentration. Under the 20 V source-drain bias, the detectivity can reach the value of 4×10^{14} Jones (Jones = $\text{cm Hz}^{1/2} \text{W}^{-1}$), which is the highest value to date compared to other report shown in Table S1.^{28-29, 41-45} The photoresponsivity and EQE are also increased to 20 A/W and 4600%, respectively. Interestingly, unlike other reports showing the decrease with the increase of laser power for the phototransistor made by 2D materials, all the figures of merit initially increase with the

enhanced illumination power and starts to decrease when the power is larger than 2000 mW/cm², shown in Figure 5(c). Besides, the 3D photoresponsivity maps shown in the Figure 5(d) and (e) indicate the notable control of photoresponse through systematically tuning the excitation power, source-drain bias and gate voltage.

To further explain the relationship between the photoresponsivity and illumination power, we further investigate the charge transfer on the interface between SnS₂ channel and graphene electrodes. The SnS₂ crystals were transferred onto the continuous graphene ribbons. Figure S4(a) schematically shows the top view and the side view of the SnS₂ on continuous graphene ribbon connected to the Cr/Au bond pads. Figure S4(b) shows the optical image of such SnS₂/graphene vertical heterostructure. Because graphene is much more conductive than the SnS₂ layers, the transfer curve of the heterostructure in Figure S4(c) shows a typical ambipolar field effect characteristic. The Dirac point at 22 V indicates the p-doping of graphene due to the exposure in the air and the PMMA transfer residual. When exposed under the laser illumination, the Dirac point of the heterostructure shifts horizontally to 16 V, indicating the graphene is less p-doped and its Fermi level is increased. This negative shift of Dirac point results from the photogenerated holes that are trapped in the SnS₂, acting as an additional positive gate voltage to graphene.⁴⁶ Figure S4(d) illustrates a schematic of band structure at the interface of graphene and SnS₂, explaining the increase of graphene Fermi level is resulted from the surface charge transfer at the heterostructure interface. Under the laser excitation, the excitons are generated in SnS₂ crystals with electrons injected into graphene and holes staying in SnS₂. This results in a decrease of work function for graphene due to its limited density of states and the Schottky barrier height at the Gr-SnS₂ junction is therefore reduced, which could lower the contact resistance at the junction and enhance the photoresponsivity of Gr-SnS₂-Gr devices.⁴⁷⁻⁴⁸ To further study the influence of illumination power on effective Schottky barrier height at the Gr-SnS₂ junction, we introduce a back-to-back Schottky diode model as a simple

representation of MSM (Gr-SnS₂-Gr) photodetector,⁴⁹ then fitting the I-V measurements under different laser power intensity using a modified thermionic emission equation (Section S1, Supporting Information). As shown in Figure S4(e), it is found that the effective Schottky barrier height greatly reduces with the increase of light power within low power density regime. When the power is larger than 2000 mW/cm², the effective Schottky barrier height remains nearly constant with a value around 0.25 V. It is manifest that the photoresponsivity increases when increasing excitation power at low power density because of the largely reduced effective Schottky barrier height, while at high power illumination the saturation of trap states and the increasing of recombination rate could lead to a decrease of photoresponsivity with the enhancement of excitation power.⁵⁰

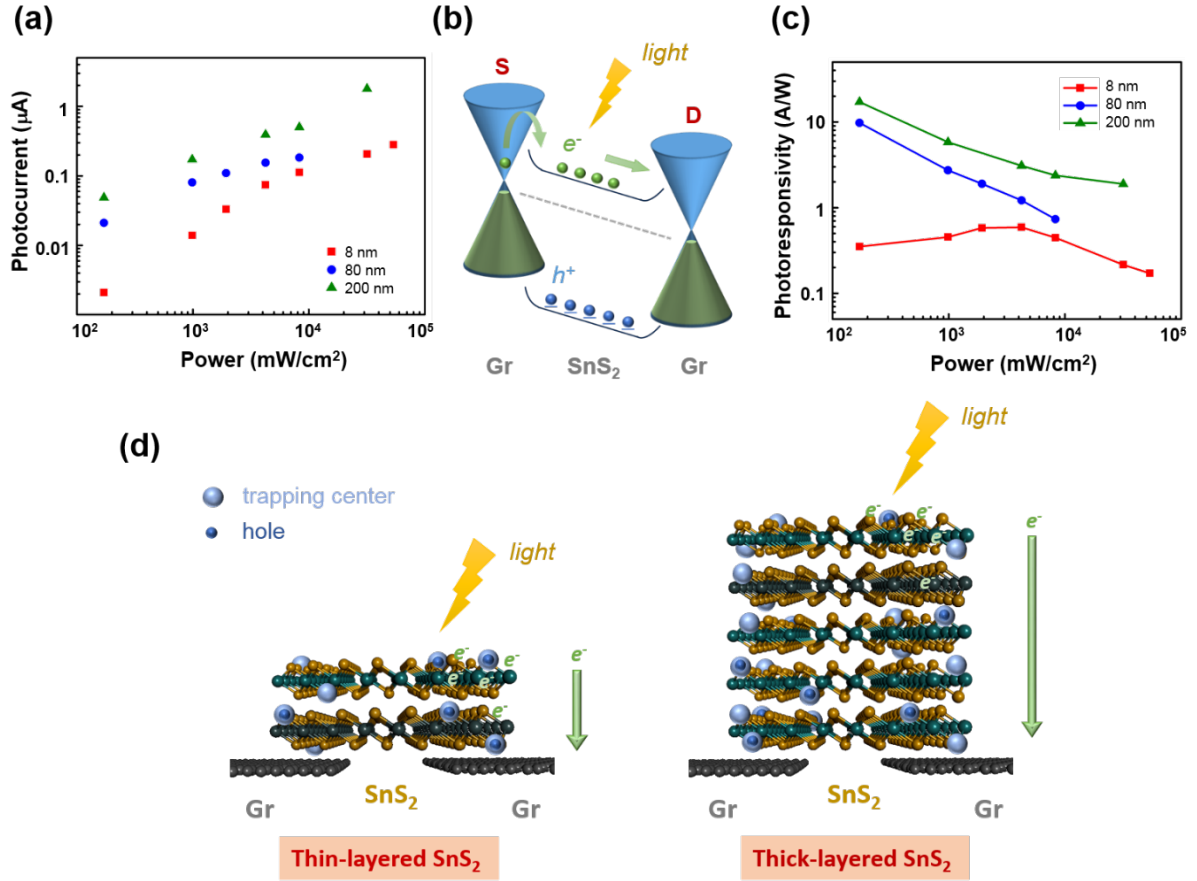


Figure 6. Influence of SnS₂ channel thickness on photoresponse behavior. (a) Power dependence of photocurrent with different SnS₂ crystal thickness under 5 V source-drain bias. (b) Energy band diagram demonstrating the photogating mechanism of the SnS₂ channel with graphene electrodes. (c) Power dependence of photoresponsivity with different SnS₂ crystal thickness under 5 V source-drain bias. (d) Schematic illustration explaining the transport mechanism of photoinduced carriers within different thickness SnS₂ channels.

To elucidate the SnS₂ crystal quality, we further measured the photoresponse on different SnS₂ channel thickness. The measured I-V characteristics and the influence excitation lower and source-drain bias on the photoresponsivity with different SnS₂ channel thickness are demonstrated in the Figure S5. Figure 6(a) shows the calculated photocurrent under the different excitation laser power. It can be seen that the photocurrent increases as the channel thickness getting larger. By fitting the plot through a simple power-law, $I_{ph} \propto P^a$, using the

relationship we can extrapolate the factor α . The sublinear dependence of photocurrent on illumination power indicates the existence of trap states, which could be resulted from the sulfur vacancies or edge defects in SnS₂ layers and the charge impurities from adsorbed molecules on the SnS₂ surface, confirming the photogating effect for the sensing mechanism with the schematic illustration demonstrated in Figure 6(b).⁵¹ In photogating effect, one of the two carrier types is trapped in the localized states located at defects or surface adsorbates, these trapped carriers act as local gates and effectively modulate the conductance of the semiconductor. As the power density increases, more surface traps may be filled by the carriers generated under illumination, thus resulting in the saturation of photocurrent. Another evidence for the presence of photogating was the substantial current spikes after turning off the laser illumination from the time-resolved curve shown in Figure 4(e). This is because of the relaxation of excessive holes staying in the trap states after switching off the laser light, the similar phenomenon has also been found by other report.⁵² In Figure 6(c), the dependence of laser power on the photoresponsivity, it can be seen that the photoresponsivity increases as SnS₂ channel become thicker under all laser illumination. It is noted that for thin SnS₂ crystals the photoresponsivity first increases with the enhancement of laser power and begins to drop at higher power density, which is due to charge transfer at the SnS₂ channel and the graphene electrodes that explained earlier. For thick SnS₂ crystals, however, the photoresponsivity decreases monotonously with the increased laser power. The reason for this is schematically explained in Figure 6(d). As SnS₂ layers become thicker, the photoinduced carrier lifetime is reduced and the influence of excitation power on photoresponse turns interface-dominant into bulk-dominant. This is due to the increasing probability of exciton interaction and diffuse path for electrons to go into graphene ribbons under laser illumination.

Conclusion

We have shown how CVD growth of SnS_2 on a SiO_2 substrate can be achieved using a combination of tin sulfide (SnS) and S powder. The as-grown SnS_2 crystals with different thickness were also incorporated with graphene electrodes grown by CVD for the fabrication of 2D photodetectors, we then investigated the photodetecting behavior of Gr- SnS_2 -Gr lateral heterostructures. For thin SnS_2 crystals, the reducing Schottky barrier height resulted from the charge transfer at the graphene- SnS_2 interface could increase the photoresponsivity with the increasing illumination power. As the SnS_2 layers become thicker, the influence turns from interface dominant into bulk dominant due to the increasing exciton interaction and the diffusion path for carriers in the SnS_2 layers. This Gr: SnS_2 :Gr 2D photodetector shows that semiconducting SnS_2 has performance comparable to other 2D TMD systems such as MoS_2 in the green spectral region when combined with graphene electrodes. This demonstrates reliable sensing properties and exhibits great potential for the future applications in ultrathin all 2D optoelectronics with high performance using SnS_2 layered crystals.

Methods

Synthesis of SnS_2

Before growth, the SiO_2 substrates were cleaned by acetone and isopropanol (IPA) for 10 min each, followed by a 5 min oxygen plasma treatment. 100 mg of sulfur powders was loaded at the center of furnace 1 in the outer 1 inch quartz tube, while 20 mg of tin sulfide (SnS) was placed at the center of furnace 2, in an inner tube with smaller diameter of 1 cm. The SiO_2 substrate was then placed downstream in the furnace 2, about 6 cm away from the SnS precursor. The CVD growth of SnS_2 was conducted at the atmospheric condition. After loading the precursors and growth substrate, the whole system was flushed with 500 sccm Ar gas for 30 min to remove the residual air and then the furnace 1 and 2 were raised to 160°C and 220°C

respectively under the 100 sccm Ar flow to create a sulfur sufficient atmosphere. After introducing sulfur vapour for 15 min, the temperature of furnace 2 was increased to 550°C and the temperature of furnace 1 was increased to 180°C to conduct the SnS₂ growth. After 15 min growth, the Ar flow rate was first decreased to 10 sccm, enabling the S molecules in the outer tube to diffuse into the inner tube and sulphurizing the SnS powder to reduce the supplied amount of SnS gaseous precursor, followed by fast cooling process with 500 sccm Ar gas flow to remove the residual gas precursors and stop the reaction.

Transfer of CVD-grown SnS₂ and graphene

After the CVD growth, the as-grown CVD samples was firstly coated with a supporting polymer film, polymethylmeth-acrylate (PMMA) at 4500 rpm for 60 seconds. The original copper substrate under the PMMA/graphene stack was then etched in 0.3 M aqueous ammonium persulfate solution; while the PMMA/SnS₂ stack on SiO₂ film was separated in 1 M aqueous potassium hydroxide solution. After the substrates were removed from the stacks by etchant solution, the stacks were then floated on DI water several times to eliminate the residual ions from etchant solution. The stacks were subsequently pasted onto other clean substrates and baked on the hot plate at 180°C for 15 min to enhance the interface contact. Finally, the PMMA supporting layer was removed by placing the sample in acetone for more than 6 hours.

Device fabrication

JEOL 5500 FS EBL system was used to pattern bond pads in a bilayer PMMA resist. A thermal evaporator was used to deposit Cr/Au (10 nm/80 nm) bond pads onto s 300 nm SiO₂/Si substrate, followed by liftoff in hot acetone. PMMA/graphene film was transferred onto the Si chip with prepatterned bond pads, and baked overnight at 180°C for better contact. Graphene film was then patterned using EBL with negative resist and oxygen plasma etching to define

graphene channels with a length and width of 100 and 25 μm , respectively. The 1 μm gaps between graphene channels were fabricated using the same process. Lastly, the PMMA/SnS₂ film was transferred to the sample.

Characterization of SnS₂-based devices

Scanning electron microscopy (SEM) was performed using a Hitachi-4300 FEG with an accelerating voltage of 3.0 kV. Raman spectroscopy was carried out using a JY Horiba LabRAM Aramis imaging confocal Raman microscope under an excitation wavelength of 532 nm at 12.5 mW power focused to a 1 μm spot size. Atomic force microscopy (AFM) was performed using an Asylum Research MFP-3D in AC mode with a silicon AC-160TS cantilever (Olympus, spring constant ~ 42 N/m and resonant frequency ~ 300 kHz). A Keithley 2400 source meter was used for I-V characteristics and responsivity of the Gr-SnS₂-Gr photodetectors. For illumination during the photoresponse measurements, a 532 nm diode-pumped solid-state laser (Thorlabs, DJ532-40) which was coupled into a confocal microscope to form a beam with spot size of $\sim 150 \mu\text{m}^2$ as a light source. The power values of the output laser are taken by a manually fixated power meter (Thorlabs Optics PM100D) placed above the devices before each I-V measurement. Tungsten tips connected to a Keithley 2400 source meter are used to probe the metal bond-pads of each devices and to apply a bias sweep from -10 V to +10 V. Measurements were all done in room-temperature under ambient pressure.

Associated content

Supporting information

Raman spectrum of Sn₂S₃ obtained from the higher growth temperature regime, Raman spectrum and corresponded step height profiles measured from atomic force microscope (AFM) for SnS₂ crystals with different thickness, Gr-SnS₂-Gr lateral heterostructure,

comparison of figure of merits with other reported photodetectors using CVD-grown two-dimensional materials as semiconducting channels, mechanism for the positive dependence on photoresponsivity with the increase of laser illumination, extraction of Schottky barrier using back-to-back diode model, thickness dependence of the source-drain current and photoresponsivity under different source-drain biased and laser illumination.

Acknowledgements

J.H.W. thanks the Royal Society and the European Research Council for support (CoG Grant 725258). R.C. acknowledges the support from Taiwan Government Scholarship to Study Abroad.

Reference

- (1) Novoselov, K. S.; Jiang, D.; Schedin, F.; Booth, T. J.; Khotkevich, V. V.; Morozov, S. V.; Geim, A. K., Two-Dimensional Atomic Crystals. *Proc. Natl. Acad. Sci. U. S. A.* **2005**, *102* (30), 10451-10453.
- (2) Novoselov, K. S.; Mishchenko, A.; Carvalho, A.; Castro Neto, A. H., 2D Materials and van der Waals Heterostructures. *Science* **2016**, *353* (6298), 9439.
- (3) Manzeli, S.; Ovchinnikov, D.; Pasquier, D.; Yazyev, O. V.; Kis, A., 2D Transition Metal Dichalcogenides. *Nat. Rev. Mater.* **2017**, *2*, 17033.
- (4) Wu, W.; Wang, L.; Li, Y.; Zhang, F.; Lin, L.; Niu, S.; Chenet, D.; Zhang, X.; Hao, Y.; Heinz, T. F.; Hone, J.; Wang, Z. L., Piezoelectricity of Single-Atomic-Layer MoS₂ for Energy Conversion and Piezotronics. *Nature* **2014**, *514* (7523), 470-474.
- (5) Schaibley, J. R.; Yu, H.; Clark, G.; Rivera, P.; Ross, J. S.; Seyler, K. L.; Yao, W.; Xu, X., Valleytronics in 2D materials. *Nat. Rev. Mater.* **2016**, *1*, 16055.
- (6) Mak, K. F.; McGill, K. L.; Park, J.; McEuen, P. L., The Valley Hall Effect in MoS₂ Transistors. *Science* **2014**, *344* (6191), 1489-1492.
- (7) Splendiani, A.; Sun, L.; Zhang, Y.; Li, T.; Kim, J.; Chim, C.-Y.; Galli, G.; Wang, F., Emerging Photoluminescence in Monolayer MoS₂. *Nano Lett.* **2010**, *10* (4), 1271-1275.
- (8) Kufer, D.; Konstantatos, G., Photo-FETs: Phototransistors Enabled by 2D and 0D Nanomaterials. *ACS Photonics* **2016**, *3* (12), 2197-2210.
- (9) Withers, F.; Del Pozo-Zamudio, O.; Mishchenko, A.; Rooney, A. P.; Gholinia, A.; Watanabe, K.; Taniguchi, T.; Haigh, S. J.; Geim, A. K.; Tartakovsky, A. I.; Novoselov, K. S., Light-Emitting Diodes by Band-Structure Engineering in van der Waals Heterostructures. *Nat. Mater.* **2015**, *14* (3), 301-306.
- (10) Lei, S.; Wen, F.; Li, B.; Wang, Q.; Huang, Y.; Gong, Y.; He, Y.; Dong, P.; Bellah, J.; George, A.; Ge, L.; Lou, J.; Halas, N. J.; Vajtai, R.; Ajayan, P. M., Optoelectronic Memory Using Two-Dimensional Materials. *Nano Lett.* **2015**, *15* (1), 259-265.
- (11) Wang, H.; Yu, L.; Lee, Y.-H.; Shi, Y.; Hsu, A.; Chin, M. L.; Li, L.-J.; Dubey, M.; Kong, J.; Palacios, T., Integrated Circuits Based on Bilayer MoS₂ Transistors. *Nano Lett.* **2012**, *12* (9), 4674-4680.
- (12) Hu, P.; Wang, L.; Yoon, M.; Zhang, J.; Feng, W.; Wang, X.; Wen, Z.; Idrobo, J. C.; Miyamoto, Y.; Geohegan, D. B.; Xiao, K., Highly Responsive Ultrathin GaS Nanosheet Photodetectors on Rigid and Flexible Substrates. *Nano Lett.* **2013**, *13* (4), 1649-1654.
- (13) Bandurin, D. A.; Tyurnina, A. V.; Yu, G. L.; Mishchenko, A.; Zólyomi, V.; Morozov, S. V.; Kumar, R. K.; Gorbachev, R. V.; Kudrynskyi, Z. R.; Pezzini, S.; Kovalyuk, Z. D.; Zeitler, U.; Novoselov, K. S.; Patané, A.; Eaves, L.; Grigorieva, I. V.; Fal'ko, V. I.; Geim, A. K.; Cao, Y., High Electron Mobility, Quantum Hall Effect and Anomalous Optical Response in Atomically Thin InSe. *Nat. Nanotechnol.* **2016**, *12*, 223-227.
- (14) Li, X.; Lin, M.-W.; Piretzky, A. A.; Idrobo, J. C.; Ma, C.; Chi, M.; Yoon, M.; Rouleau, C. M.; Kravchenko, I. I.; Geohegan, D. B.; Xiao, K., Controlled Vapor Phase Growth of Single Crystalline, Two-Dimensional GaSe Crystals with High Photoresponse. *Sci. Rep.* **2014**, *4*, 5497.

- (15) Mutlu, Z.; Wu, R. J.; Wickramaratne, D.; Shahrezaei, S.; Liu, C.; Temiz, S.; Patalano, A.; Ozkan, M.; Lake, R. K.; Mkhoyan, K. A.; Ozkan, C. S., Phase Engineering of 2D Tin Sulfides. *Small* **2016**, *12* (22), 2998-3004.
- (16) Debtanu, D.; John, M.; Sean, S.; Vincent, Z.; Arnold, G.; Haibing, P., High On/Off Ratio Field Effect Transistors Based on Exfoliated Crystalline SnS₂ Nano-Membranes. *Nanotechnology* **2013**, *24* (2), 025202.
- (17) Ou, J. Z.; Ge, W.; Carey, B.; Daeneke, T.; Rotbart, A.; Shan, W.; Wang, Y.; Fu, Z.; Chrimes, A. F.; Wlodarski, W.; Russo, S. P.; Li, Y. X.; Kalantar-zadeh, K., Physisorption-Based Charge Transfer in Two-Dimensional SnS₂ for Selective and Reversible NO₂ Gas Sensing. *ACS Nano* **2015**, *9* (10), 10313-10323.
- (18) Lee, M.-J.; Ahn, J.-H.; Sung, J. H.; Heo, H.; Jeon, S. G.; Lee, W.; Song, J. Y.; Hong, K.-H.; Choi, B.; Lee, S.-H.; Jo, M.-H., Thermoelectric Materials by Using Two-Dimensional Materials with Negative Correlation Between Electrical and Thermal Conductivity. *Nat. Commun.* **2016**, *7*, 12011.
- (19) Chao, D.; Liang, P.; Chen, Z.; Bai, L.; Shen, H.; Liu, X.; Xia, X.; Zhao, Y.; Savilov, S. V.; Lin, J.; Shen, Z. X., Pseudocapacitive Na-Ion Storage Boosts High Rate and Areal Capacity of Self-Branched 2D Layered Metal Chalcogenide Nanoarrays. *ACS Nano* **2016**, *10* (11), 10211-10219.
- (20) Raffone, F.; Ataca, C.; Grossman, J. C.; Cicero, G., MoS₂ Enhanced T-Phase Stabilization and Tunability Through Alloying. *J. Phys. Chem. Lett.* **2016**, *7* (13), 2304-2309.
- (21) Sutter, E.; Huang, Y.; Komsa, H. P.; Ghorbani-Asl, M.; Krasheninnikov, A. V.; Sutter, P., Electron-Beam Induced Transformations of Layered Tin Dichalcogenides. *Nano Lett.* **2016**, *16* (7), 4410-4416.
- (22) Ahn, J.-H.; Lee, M.-J.; Heo, H.; Sung, J. H.; Kim, K.; Hwang, H.; Jo, M.-H., Deterministic Two-Dimensional Polymorphism Growth of Hexagonal n-Type SnS₂ and Orthorhombic p-Type SnS Crystals. *Nano Lett.* **2015**, *15* (6), 3703-3708.
- (23) Huang, Y.; Sutter, E.; Sadowski, J. T.; Cotlet, M.; Monti, O. L. A.; Racke, D. A.; Neupane, M. R.; Wickramaratne, D.; Lake, R. K.; Parkinson, B. A.; Sutter, P., Tin Disulfide—An Emerging Layered Metal Dichalcogenide Semiconductor: Materials Properties and Device Characteristics. *ACS Nano* **2014**, *8* (10), 10743-10755.
- (24) Tao, Y.; Wu, X.; Wang, W.; Wang, J., Flexible Photodetector from Ultraviolet to Near Infrared Based on a SnS₂ Nanosheet Microsphere Film. *J. Mater. Chem. C* **2015**, *3* (6), 1347-1353.
- (25) Rong, Y.; Fan, Y.; Leen Koh, A.; Robertson, A. W.; He, K.; Wang, S.; Tan, H.; Sinclair, R.; Warner, J. H., Controlling Sulphur Precursor Addition for Large Single Crystal Domains of WS₂. *Nanoscale* **2014**, *6* (20), 12096-12103.
- (26) Shanshan, W.; Merce, P.; Harish, B.; Jamie, H. W., Substrate Control for Large Area Continuous Films of Monolayer MoS₂ by Atmospheric Pressure Chemical Vapor Deposition. *Nanotechnology* **2016**, *27* (8), 085604.
- (27) Sheng, Y.; Tan, H.; Wang, X.; Warner, J. H., Hydrogen Addition for Centimeter-Sized Monolayer Tungsten Disulfide Continuous Films by Ambient Pressure Chemical Vapor Deposition. *Chem. Mater.* **2017**, *29* (11), 4904-4911.

- (28) Xia, J.; Zhu, D.; Wang, L.; Huang, B.; Huang, X.; Meng, X.-M., Large-Scale Growth of Two-Dimensional SnS₂ Crystals Driven by Screw Dislocations and Application to Photodetectors. *Adv. Funct. Mater.* **2015**, *25* (27), 4255-4261.
- (29) Zhou, X.; Zhang, Q.; Gan, L.; Li, H.; Zhai, T., Large-Size Growth of Ultrathin SnS₂ Nanosheets and High Performance for Phototransistors. *Adv. Funct. Mater.* **2016**, *26* (24), 4405-4413.
- (30) Song, H. S.; Li, S. L.; Gao, L.; Xu, Y.; Ueno, K.; Tang, J.; Cheng, Y. B.; Tsukagoshi, K., High-Performance Top-Gated Monolayer SnS₂ Field-Effect Transistors and Their Integrated Logic Circuits. *Nanoscale* **2013**, *5* (20), 9666-9670.
- (31) Hu, Y.; Chen, T.; Wang, X.; Ma, L.; Chen, R.; Zhu, H.; Yuan, X.; Yan, C.; Zhu, G.; Lv, H.; Liang, J.; Jin, Z.; Liu, J., Controlled Growth and Photoconductive Properties of Hexagonal SnS₂ Nanoflakes with Mesa-Shaped Atomic Steps. *Nano Res.* **2017**, *10* (4), 1434-1447.
- (32) Price, L. S.; Parkin, I. P.; Hardy, A. M. E.; Clark, R. J. H.; Hibbert, T. G.; Molloy, K. C., Atmospheric Pressure Chemical Vapor Deposition of Tin Sulfides (SnS, Sn₂S₃, and SnS₂) on Glass. *Chem. Mater.* **1999**, *11* (7), 1792-1799.
- (33) Smith, A. J.; Meek, P. E.; Liang, W. Y., Raman Scattering Studies of SnS₂ and SnSe₂. *J. Phys. C: Solid State Phys.* **1977**, *10* (8), 1321-1323.
- (34) Xia, J.; Li, X.-Z.; Huang, X.; Mao, N.; Zhu, D.-D.; Wang, L.; Xu, H.; Meng, X.-M., Physical Vapor Deposition Synthesis of Two-Dimensional Orthorhombic SnS Flakes with Strong Angle/Temperature-Dependent Raman Responses. *Nanoscale* **2016**, *8* (4), 2063-2070.
- (35) Gonzalez, J. M.; Oleynik, I. I., Layer-Dependent Properties of SnS₂ and SnSe₂ Two-Dimensional Materials. *Phys. Rev. B* **2016**, *94* (12), 125443.
- (36) Yu, Y.-J.; Zhao, Y.; Ryu, S.; Brus, L. E.; Kim, K. S.; Kim, P., Tuning the Graphene Work Function by Electric Field Effect. *Nano Lett.* **2009**, *9* (10), 3430-3434.
- (37) Burton, L. A.; Whittles, T. J.; Hesp, D.; Linhart, W. M.; Skelton, J. M.; Hou, B.; Webster, R. F.; O'Dowd, G.; Reece, C.; Cherns, D.; Fermin, D. J.; Veal, T. D.; Dhanak, V. R.; Walsh, A., Electronic and Optical Properties of Single Crystal SnS₂: an Earth-Abundant Disulfide Photocatalyst. *J. Mater. Chem. A* **2016**, *4* (4), 1312-1318.
- (38) Lopez-Sanchez, O.; Lembke, D.; Kayci, M.; Radenovic, A.; Kis, A., Ultrasensitive Photodetectors Based on Monolayer MoS₂. *Nat. Nanotechnol.* **2013**, *8* (7), 497-501.
- (39) Renteria, J.; Samnakay, R.; Rumyantsev, S. L.; Jiang, C.; Goli, P.; Shur, M. S.; Balandin, A. A., Low-Frequency 1/f Noise in MoS₂ Transistors: Relative Contributions of the Channel and Contacts. *Appl. Phys. Lett.* **2014**, *104* (15), 153104.
- (40) Kufer, D.; Konstantatos, G., Highly Sensitive, Encapsulated MoS₂ Photodetector with Gate Controllable Gain and Speed. *Nano Lett.* **2015**, *15* (11), 7307-7313.
- (41) Tsai, D.-S.; Liu, K.-K.; Lien, D.-H.; Tsai, M.-L.; Kang, C.-F.; Lin, C.-A.; Li, L.-J.; He, J.-H., Few-Layer MoS₂ with High Broadband Photogain and Fast Optical Switching for Use in Harsh Environments. *ACS Nano* **2013**, *7* (5), 3905-3911.
- (42) Zhang, W.; Chiu, M.-H.; Chen, C.-H.; Chen, W.; Li, L.-J.; Wee, A. T. S., Role of Metal Contacts in High-Performance Phototransistors Based on WSe₂ Monolayers. *ACS Nano* **2014**, *8* (8), 8653-8661.

- (43) Ye, G.; Gong, Y.; Lei, S.; He, Y.; Li, B.; Zhang, X.; Jin, Z.; Dong, L.; Lou, J.; Vajtai, R.; Zhou, W.; Ajayan, P. M., Synthesis of Large-Scale Atomic-Layer SnS₂ Through Chemical Vapor Deposition. *Nano Res.* **2017**, *10* (7), 2386-2394.
- (44) Su, G.; Hadjiev, V. G.; Loya, P. E.; Zhang, J.; Lei, S.; Maharjan, S.; Dong, P.; M. Ajayan, P.; Lou, J.; Peng, H., Chemical Vapor Deposition of Thin Crystals of Layered Semiconductor SnS₂ for Fast Photodetection Application. *Nano Lett.* **2015**, *15* (1), 506-513.
- (45) Huang, Y.; Deng, H.-X.; Xu, K.; Wang, Z.-X.; Wang, Q.-S.; Wang, F.-M.; Wang, F.; Zhan, X.-Y.; Li, S.-S.; Luo, J.-W.; He, J., Highly Sensitive and Fast Phototransistor Based on Large Size CVD-grown SnS₂ Nanosheets. *Nanoscale* **2015**, *7* (33), 14093-14099.
- (46) Zhang, W.; Chuu, C.-P.; Huang, J.-K.; Chen, C.-H.; Tsai, M.-L.; Chang, Y.-H.; Liang, C.-T.; Chen, Y.-Z.; Chueh, Y.-L.; He, J.-H.; Chou, M.-Y.; Li, L.-J., Ultrahigh-Gain Photodetectors Based on Atomically Thin Graphene-MoS₂ Heterostructures. *Sci. Rep.* **2014**, *4*, 3826.
- (47) Tan, H.; Fan, Y.; Rong, Y.; Porter, B.; Lau, C. S.; Zhou, Y.; He, Z.; Wang, S.; Bhaskaran, H.; Warner, J. H., Doping Graphene Transistors Using Vertical Stacked Monolayer WS₂ Heterostructures Grown by Chemical Vapor Deposition. *ACS Appl. Mater. Interfaces* **2016**, *8* (3), 1644-1652.
- (48) Tan, H.; Fan, Y.; Zhou, Y.; Chen, Q.; Xu, W.; Warner, J. H., Ultrathin 2D Photodetectors Utilizing Chemical Vapor Deposition Grown WS₂ With Graphene Electrodes. *ACS Nano* **2016**, *10* (8), 7866-7873.
- (49) Fan, Y.; Zhou, Y.; Wang, X.; Tan, H.; Rong, Y.; Warner, J. H., Photoinduced Schottky Barrier Lowering in 2D Monolayer WS₂ Photodetectors. *Adv. Opt. Mater.* **2016**, *4* (10), 1573-1581.
- (50) Zhang, W.; Huang, J.-K.; Chen, C.-H.; Chang, Y.-H.; Cheng, Y.-J.; Li, L.-J., High-Gain Phototransistors Based on a CVD MoS₂ Monolayer. *Adv. Mater.* **2013**, *25* (25), 3456-3461.
- (51) Island, J. O.; Blanter, S. I.; Buscema, M.; van der Zant, H. S. J.; Castellanos-Gomez, A., Gate Controlled Photocurrent Generation Mechanisms in High-Gain In₂Se₃ Phototransistors. *Nano Lett.* **2015**, *15* (12), 7853-7858.
- (52) Ma, S.; Zeng, L.; Tao, L.; Tang, C. Y.; Yuan, H.; Long, H.; Cheng, P. K.; Chai, Y.; Chen, C.; Fung, K. H.; Zhang, X.; Lau, S. P.; Tsang, Y. H., Enhanced Photocatalytic Activity of WS₂ Film by Laser Drilling to Produce Porous WS₂/WO₃ Heterostructure. *Sci. Rep.* **2017**, *7* (1), 3125.

TOC

